Appendix F

Estimated Changes in State on San Francisco Bay Region Faults Resulting from the 1906 and 1989 Earthquakes

Robert W. Simpson

Introduction

In the 70 years prior to the great 1906 San Francisco earthquake, seventeen **M**≥6 earthquakes shook the San Francisco Bay region; in the 94 years following there have been only five (Bakun, 1999). A plausible explanation is that after great earthquakes the crust in an entire region is relaxed, creating a "stress shadow" within which other large earthquakes are suppressed until plate tectonic stresses gradually reload the faults (Ellsworth and others, 1981; Harris and Simpson, 1998). Calculations indicate that every major fault system in the Bay region was relaxed to some degree by the 1906 event (Figure 1).

In this report, calculated changes in stress are *static* changes, which are the changes that persist after the passage of the seismic waves with their attendant *dynamic* stress changes. Dynamic stress changes are often considerably larger than static changes, although dynamic changes may have the greatest effect on faults that were already close to failure, whereas static changes would have a greater long-term role in advancing or delaying future earthquakes on faults not yet near the end of their loading cycle (e.g., Kilb and others, 2000).

Calculations of stress changes were made by assuming elastic halfspace behavior and using rectangular dislocations to represent slipping fault segments (Okada, 1992). Although the elastic assumption probably does a fair job of estimating coseismic stress changes immediately after an earthquake, it cannot adequately describe post-seismic relaxation caused by viscous flow in the lower crust and mantle (e.g., Pollitz and others, 1998; Kenner and Segall, 1999) and it offers a limited number of ways to simulate tectonic loading on faults, which may result in estimated loading rates that are too large (Parsons, 2001). At the time WG99 began, it seemed safest to use the simple elastic halfspace approach in spite of its shortcomings, because more complex models did not seem fully mature and required additional assumptions about rheology and geometry.

The conceptual approach to failure used in this report is based on the Coulomb failure criterion: a stress relaxation shadow delays future earthquakes on a fault at least until the state of stress on the fault recovers to its pre-1906 level (Figure 2), at which time the possibility of an earthquake occurring once again exists. Laboratory derived rate-and-state failure laws suggest that changes in the timing of failure are not this simple—especially if the fault was close to failure just before it was relaxed (e.g., Dieterich, 1994; Stein and others, 1998; Gomberg and others, 1998; Harris and Simpson, 1998; Toda and others, 1998). Rate-and-state approaches to the estimation of earthquake-induced probability changes are being actively researched and tested (e.g., Dieterich and others, 2000; Gomberg and others, 2000; Parsons and others, 2000; Toda and Stein, 2001), but for the purposes of this report, the simple Coulomb failure approach was deemed most appropriate, pending further validation of the newer methods.

The Coulomb failure approach used here assumes a fixed failure threshold to estimate a *clock change* in years (Figure 2). Calculation of a clock change requires information about (1) the

coseismic Coulomb stress change on the fault and (2) the long-term loading rate of the fault caused by plate tectonic displacements. The clock change equals the coseismic stress change (in bars) divided by the loading rate (in bars/yr), and can be either a delay in the case of relaxation or an advance if Coulomb failure stress has been increased. This clock change can then be used to adjust probability estimates.

Two adjustment approaches were tried in conjunction with the Brownian Passage Time (BPT) probability distribution: Originally the estimated clock change was used to shift the reset time of the last event on a segment forward or backward by that number of years depending on whether the change was relaxing or more stressing. But the BPT distribution is based on a physical concept of a state evolving in time toward a failure threshhold, and this affords a natural way to perturb the system by stepping the state closer to or farther from the failure threshhold. Although the original approach of shifting reset times was easy to implement, it offers a good approximation to the BPT state-step result only if the time elapsed since the last event is small compared with the recurrence interval for the segment. Unfortunately, this condition was not met by many segments. We ultimately implemented the BPT state-step approach in order to overcome this limitation. Step size was estimated from the clock change and the recurrence interval. (See other appendices describing the BPT distribution for details.)

The question of immediate concern is whether the period of post-1906 quiescence can be expected to continue in the Bay region, or whether it has ended for at least some faults. Simple models described here indicate that most faults in the Bay region, with perhaps the exception of the northern San Gregorio fault, have recovered from the relaxation and passed the level of stressing that obtained for them just before the 1906 event. In spite of the uncertainties in these models and the difficulties in confirming and calibrating their results, it would seem prudent to act on the assumption that the extraordinary period of seismic quiet experienced in the Bay area after 1906 is ended or close to ending.

Coulomb Stress Change

The Coulomb stress change at a point on a fault surface is calculated using the Coulomb failure criterion (Jaeger and Cook, 1979; Scholz, 1990), which says that a fault will fail when the shear and normal stresses on the surface satisfy:

$$\sigma_C \equiv \tau - \mu(\sigma_n - p) \geq C \qquad (1)$$

where τ is the magnitude of the shear stress acting on the fault plane, μ is the coefficient of friction, σ_n is the normal stress acting on the fault plane (positive in compression), p is the pore fluid pressure, and C is the cohesion. The quantity on the left of the inequality is called the Coulomb stress σ_C (also referred to as the Coulomb failure function or CFF). Assuming that the cohesion C does not change, then a stress change induced by a nearby earthquake or other source can move the fault closer to or farther from failure depending on whether the sign of the change in Coulomb stress is positive or negative:

$$\Delta\sigma_C = \Delta\tau_r - \mu(\Delta\sigma_n - \Delta p) \qquad (2)$$

where $\Delta\tau_r$ indicates the shear stress change in the rake (slip) direction of the fault, which implies that the important shear stresses are those that act in the usual slip direction of the fault.

Changes in pore fluid pressure in response to changes in the local stress tensor depend on the poroelastic behavior of the fault zone and surrounding materials. If there are permeable pathways for the fluid to migrate Δp will also evolve with time as the fluid re-equilibrates to the new stress regime (Jaumé and Sykes, 1992). Two fluid behavior models that are commonly used assume either (1) that the instantaneous changes in pore pressure follow isotropic homogeneous poroelastic behavior or (2) respond in linear fashion to the normal stress changes (Roeloffs, 1996; Beeler and others, 2000). Little is know about the evolution in time of pore fluid pressures, although it has been suggested that it might be a combination of such behaviors (Rice and Cocco, 2000). It seems fair to say that existing models of pore fluid behavior, based as they are on very limited observations, probably fall far short of describing the real complexity that exists in the earth.

Estimating 1906 Coseismic Coulomb Stress Changes

Coseismic static stress changes on Bay region faults were estimated for the great 1906 San Francisco earthquake and for the 1989 Loma Prieta earthquake. Many examples of such calculations, designed to investigate stress triggering of earthquakes and the locations of aftershocks after a large mainshock, have been reviewed by Harris (1998). For the models described here, the stress changes were obtained using the elastic-halfspace dislocation equations of Okada (1992). These equations apply to rectangular dislocation patches, which can be arranged end-to-end to represent an earthquake rupture.

Because little is presently known about the appropriate values for coefficient of friction and other parameters, and because of uncertainties in the endpoints and heights of the WG99 segments, a Monte Carlo approach was adopted to explore a range of weighted possibilities. Estimation of the change in Coulomb failure stress on a fault requires a value for the coefficient of friction, which determines the relative contribution of fault-normal stress changes to failure, and an assumption as to how pore fluid behavior modulates the stress changes. Choices and weights used here for these parameters are given in the first 3 rows of Table 1.

The 1906 rupture model of Thatcher and others (1997) used an array of 10-km tall by 10-km long rectangular patches to represent the 480-km long earthquake fault plane (Figure 1). Their model was based on an analysis of geodetic observations before and after the event and offers uncertainties that define the range of probable slip values consistent with the observations. These uncertainties were used to define "minimum" and "maximum" slip distributions for the 1906 event ("Slip Distribution" parameter in Table 1). The depth of rupture was poorly resolved by inversion of the geodetic data, so depths of 10 km and 15 km were used ("Rupture depth" parameter in Table 1). The 15 km depth also allows, in an approximate way, for the possibility of aseismic afterslip on and under the 1906 rupture patches, which took place in the months and years after 1906 (Kenner and Segall, 2000; Parsons, 2001) and might have helped to further relax nearby faults.

Coseismic stress changes were calculated at the centers of WG99 segments. This approach worked for the 1906 earthquake, because almost all WG99 segments, with the exception of the San Gregorio North (SGN) and the Calaveras South (CS), are far enough removed from the 1906 rupture that there is not a great variation in coseismic stress change from one end of a segment to

the other. Calculations in which the WG99 segments were divided into ~10-km sub-segments offered greater resolution along segments, but the added model complexity did not seem warranted given the many uncertainties in parameter values and in the validity of the elastic-halfspace approach itself. Moreover, the resulting clock-change estimates, reported in WG99 (1999), were not notably different from those obtained using the segment-center approach described here.

The Monte Carlo approach was implemented in two steps. Norm Abrahamson generated 10,000 instances of Bay region fault-segment geometries, slip rates, and R-factors using the values, weights, and constraints assigned by WG99. For each instance, a rupture geometry, a rupture slip distribution, a coefficient of friction, a pore model, and other parameters were selected using the weights shown in Table 1. The coseismic stress change, loading-rate (as described in the next section), and finally a clock change were calculated for each instance using these choices, resulting in a distribution of 10,000 clock changes (Table 2).

Estimating Tectonic Loading Rates

In order to estimate the impact of these coseismically-induced stress changes on Bay region faults, we need to know the long-term loading rate on these faults caused by plate tectonic motion of the Pacific plate relative to the Sierra Nevada plate. There are two traditional ways to arrive at a loading rate in elastic halfspace models, both requiring knowledge of the long-term slip rates of the faults in question.

The first "deep slip" approach assumes that below its seismogenic locked part a fault segment continues to extend downward to great depth. This extension is assumed to be slipping continuously and aseismically at some long-term rate, because the temperatures and rheologies at these depths favor continuous deformation over brittle failure. As the deep section slips it loads additional stress onto the locked patch above and other nearby locked patches. Implementing this approach with dislocations requires that the deep extensions to the faults continue well beyond the study area, because the effect of these deep dislocations is felt at considerable distances. Problems arise at locations where two or more segments join but a discontinuity in long-term slip rates exists at the join, because such discontinuities create large stress and strain anomalies. (In the real world, such discontinuities produce local deformation including folds and ancillary faults.)

The second "virtual dislocation" approach (e.g., Jaumé and Sykes, 1996; Deng and Sykes, 1997; Ward, 2000) can be shown to be equivalent to the deep slip approach in two-dimensional geometries. In the virtual dislocation approach, loading is estimated by forcing the locked patches to slip backwards (that is, in a left-lateral sense for the Bay region) at the observed long-term slip rate. There is no long-term buildup of stress anywhere in the model, as can happen in the “deep slip” approach, because earthquakes occurring on the segments will, in the long-term exactly balance the reverse loading displacement. Virtual dislocation loading is less prone to end effects and join problems because the dislocations are smaller, and was adopted for the present calculations because both these problems exist in the WG99 segmentation model for the Bay region.

For each of the 10,000 instances, the same values for coefficient of friction and pore model parameters were used to calculate loading rates as in the coseismic stress change calculation described in the previous section. It seems likely that different pore models would apply over the long term and short term, corresponding to drained and undrained states (e.g., Rice and Cocco,

2000), but such a modification will probably not change the results greatly given the choice and weights of pore models used here.

Alternate models for loading of Bay region faults based on finite-element computations using more realistic rheologies are discussed briefly in a later section. At least one of these models gives systematically lower loading rates than those calculated here (Parsons, 2001). These alternate loading scenarios are not used here, but should be considered by future working groups.

Seismogenic Scaling Factors (R-Factors)

Some faults in the Bay region are creeping more or less continuously at the surface, and others may have regions of aseismic creep at depth. Because the moment released by such aseismic slip is not available for release in earthquakes, WG99 has assigned to each Bay region fault segment a seismogenic scaling factor or *R-factor* value:

> To account for observed aseismic slip (creep) on some faults in the SFBR, a seismic slip factor, also known as the seismic coupling factor, was introduced in the model. A segment with a seismic slip factor of R=1 accumulates seismic moment at the full geologic rate, while a segment with a factor of R=0 releases all of its geologic moment through creep. The seismic slip factor was used to define the area of the fault that stores seismic moment, thereby affecting both the amount of seismic moment released in a rupture and the mean rate of ruptures on a segment, but not the long-term fault slip rate. (WG99, 1999)

Although this definition seems straightforward enough as applied to the long-term, there are a number of complications that are not immediately obvious. In order to estimate an R-factor for a fault segment, it is usually necessary to recast the definition in terms of what we know from geodesy and geology about the present (interseismic) creep rate and long-term slip rate on a fault segment. If $r \equiv (G-S)/G$ where G is the long-term geologic slip rate and S is the current interseismic slip rate inferred from geodesy, then in general $R \neq r$ because S changes through the seismic cycle. (G may change over time too, but is assumed to be constant in this discussion.) For example, one can imagine creeping faults, driven additionally by slip at depth under adjacent faults during interseismic parts of the cycle so that $S>G$, yielding negative r values (e.g., Savage and Lisowski, 1993; Simpson and others, 2001).

One of the more perplexing problems in applying R-factors to the calculation of clock changes is that the geometry of slipping regions and locked patches makes a considerable difference in estimated loading rates. If the locked patches are concentrated on the deeper parts of a fault segment, loading rates are quite different than if the lock patches are concentrated toward one end of the segment. The creeping parts of a fault segment (for $R<1$) will presumably also respond to a coseismic stress change over time, in general further relaxing locked patches that were relaxed and further loading patches that were loaded, so that the clock change for a given segment will vary with time. Another oddity lies in the fact that even though, for example, half of a fault segment may be free to slip area-wise, the adjacent locked patches occupying the other half of the segment and locked patches on neighboring segments will retard creep on the freely slipping half. When any of these locked patches fail in an earthquake, is it safe to assume that the moment stored in the retarded creep on creeping half will not be released, at least in part, coseismically? Examples offered in Appendix R illustrate some of these behaviors.

Because of these problems and uncertainties as to the real behavior of creeping faults, it was decided once again that the best course was the simplest. For that reason, WG99 R-factors were

applied directly to calculated clock changes by multiplication to yield final clock changes described in the next section (Appendix R, Figure R2). Test runs in which R-factors were applied to loading rates, or in which a range of three different weighted R-factors were applied yielded results that were not different enough to justify the added complexity.

Estimating 1906 Clock Changes and Uncertainties

Assuming a steady loading rate in units of bars/yr and a known coseismic stress relaxation in units of bars, the duration of relaxation in the Coulomb approach is the coseismic step divided by the loading rate. (This assumes that the earthquake-induced stress change and associated shaking have not affected the failure process, the Coulomb failure threshold, the fault strength, the pore fluids, or the loading process in some complicated way.)

For each of the 10,000 instances, a clock change was calculated by carrying out this division. One problem that emerges is that sometimes for a given combination of variables the estimated loading rate is very small (positive or negative), leading to a clock change that is very large (positive or negative). It is unlikely that the simple elastic approach presented here could remain correct over periods of hundreds or thousands of years, so such results are not considered meaningful. Although such values represent less than 10% of the total instances, they do bias the calculation of average values and standard deviations. For that reason, median (rather than average) values are reported in Table 2, and values at the 5- and 95-percentiles are used as 90% confidence bounds.

Comparison with Earlier Results and with Other R-factor Assumptions.

Differences between the clock changes values listed in Table 2 and previous published values (Table 6, WG99, 1999) result from the earlier estimates (1) using 10-km sub-segments, (2) ignoring R-factors values, (3) neglecting height and width uncertainties for WG99 segments, and (4) using maximum and minimum values as uncertainty bounds, rather than the 90% confidence bounds in Table 2. These differences and the R-factors used are shown in Table 3. In general, applying the R-factor directly to the uncorrected clock change produces results comparable to those found by applying the adjustment to loading rate.

Estimating 1989 Clock Changes

For the 1989 Loma Prieta earthquake, calculating coseismic stress changes at the centers of WG99 segments worked adequately for most segments, but failed to yield meaningful results for the Santa Cruz (SAS) and Peninsula (SAP) segments of the San Andreas fault immediately adjacent to the Loma Prieta earthquake rupture. Although segments at intermediate distances (HS, CC, CS, SGS, SGN) showed some variation in coseismic stress changes along their lengths, the stress change values were in general small enough on these segments that the variation could be safely ignored. The two segments adjacent to the rupture (SAS and SAP) experienced extremely large variations in coseismic stress change along their lengths and also in the vertical dimension, so that the values at the WG99 centers were essentially meaningless (Figure LP1). These very large variations in calculated stresses over the surfaces of SAS and SAP depend critically on the distance from the rupture and also on the details of the rupture model used. In order to better sample the range of coseismic stress change values on SAS and SAP, we

constructed a more detailed model of these fault segments with 2-km rectangular patches. The special ad hoc treatment applied to these two segments is described in detail in Appendix LP.

Three published rupture models for the Loma Prieta event were used in the calculation applied to WG99 centers as well as in the special calculation for SAS and SAP. The weights given to these three models are shown in the last row of Table 1. The results of the initial calculation using the centers of WG99 segments are listed in Table 4. The combined results with special values added for SAS and SAP are shown in Table 5. It appears that for most segments, the clock change values are small. Previous estimates of the clock change on the southernmost part of the southern Hayward fault yielded an estimate of ~6 years (Lienkaemper and others, 1997), suggesting that the HS segment might also have profited from special treatment. The preferred value for SAP in Table 5 is close to zero, but the large confidence bounds reflect the variations over the surface of this segment, as is also true of SAS (see Appendix LP for details). Although both these segments have parts that were highly stressed, it is uncertain what the ultimate impact of this stressing might be, since we have no information as to where the hypocenter of the next large event on these segments might lie. It is possible that in the absence of the Loma Prieta event, the next earthquake on one of these segments might have nucleated at one of the spots that were strongly relaxed. It that case, the next event could have been delayed by 1989. The large uncertainty bounds placed on the 1989 clock changes for these segments reflect some of these problems.

Applying 1906 and 1989 Clock Changes as BPT state steps

A summary of preferred clock changes and confidence bounds for the 1906 San Francisco and 1989 Loma Prieta earthquakes is given in Table 6. For 30-year periods beginning after 1906 but before 1989, only the 1906 clock changes should be used as input to Norm Abrahamson's program. For 30-year intervals beginning after 1989, perturbations from both earthquakes should be included. For our original approach using the clock change to shift the reset time of the last event, the timing of the perturbations was not a factor and the two clock changes were added and the reset time of the last event on a segment was shifted by the clock change to a later date if the segment was relaxed and to an earlier date if more stressed. However, as mentioned earlier, this approach was abandoned when it proved to be a poor approximation to the more natural approach in the context of the BPT distribution of stepping BPT state closer or farther from the failure threshhold.

For the "BPT state shift" approach which we ultimately used, the fractional shift in state needs to be calculated separately for each event from its estimated clock change and segment recurrence interval and applied to the BPT state at the appropriate time. Unfortunately, limitations in the program permitted only one state shift per segment in a given run. We worked around this limitation by applying the 1906 state shift to non-San Andreas segments (where 1906 typically had a much larger effect) and the 1989 state shift to two San Andreas segments—the Santa Cruz (SAS) and Peninsula (SAP) segments—where 1989 had a large impact. (San Gregorio South and Mt. Diablo segments had somewhat comparable shifts in both events, but this is not likely to change the overall results greatly.)

A potential inconsistency arises from using the clock change results as input to the Norm Abrahamson program. Ideally, a clock change would be estimated within his program for each instance as it arose using the parameters selected for that instance (although this would add a considerable computational burden to an already complicated program). Otherwise, applying the same tabulated clock changes and confidence bounds to every instance, as was done, could result in a bias caused by potentially strong correlation of the clock changes with certain parameter

values. For example, if the clock changes on a segment were strongly correlated with R-factor values, then it would be inappropriate to select the upper-confidence clock-change value for an instance with a low R-factor. In future efforts, such correlations should also be tabulated, or a cleaner integration of the clock change results into the master program should be considered. One approach would be to tabulate the clock changes by instance and read them into the master program as input, assuming that the relevant instance parameters were specified in advance.

Discussion, Alternate Approaches, and Problems

The confidence bounds given in the various tables reflect the range of possible values that derive from different assumed model parameters. Thus they are measures of uncertainty *relative* to the elastic-halfspace dislocation model used here to calculate these clock changes. The model itself is open to criticism. To name just a few of its shortcomings: (1) It assumes that the earth behaves like an elastic halfspace over periods of decades to centuries, (2) it uses a simple but unlikely mechanism for long-term tectonic loading of the faults, and (3) it averages stress changes over broad segment-surfaces which hides the stress concentrations around individual asperities and locked patches where earthquakes likely nucleate. Ideally, future working group efforts should include estimates from more than one interaction model using different approaches and exploring different physical behaviors and rheologies.

Elastic dislocation models of the stress changes on San Francisco Bay region faults induced by the 1906 event suggest that the relaxation would typically last for decades, depending on the location and distance of the fault from the 1906 rupture (Simpson and Reasenberg, 1994; Jaumé and Sykes, 1996). It seems unlikely that the Earth is going to behave as an elastic medium over a time span of decades, but the current uncertainties in assigning geometries and parameters to more complex models argue in favor of simplicity. Afterslip, aseismic slip on horizontal detachment faults, viscous relaxation in the lower crust, and a host of other possible effects may increase or decrease the clock changes estimated here. In fact the observed seismic quiescence in the Bay region for 70 or more years after 1906 is longer than most estimates based on elastic halfspace models by a factor of 2 or more, suggesting that elastic models based on 1906 coseismic stress changes are not capturing all of the physical processes at play.

Simpson and Reasenberg (1994) attempted to estimate the magnitude of stress changes that would be produced by viscous relaxation on a horizontal detachment at depth after the 1989 Loma Prieta earthquake. Their model suggested that the 1989 coseismic stress changes on some of the Bay region faults might be amplified by a factor of two as the limit of viscous relaxation was reached. Linker and Rice (1997, Fig.5) found that the biggest amplification occurs at the south end of the SAP segment, just north of the rupture, with factors of approximately 4-7 depending on the model used. Kenner and Segall (1999) investigated post-seismic deformation and its effects on stress relaxation after a 1906-size earthquake using 2-dimensional viscoelastic models of the crust and mantle. They concluded that viscoelastic relaxation could over time amplify the effect of the relaxation on the Hayward fault by a factor six for a detachment geometry, increasing the duration of the stress shadow in the vicinity of the Hayward fault by a factor of ~3. Parsons (2001) used a 3-dimensional finite element model to study the loading and interaction of Bay region faults and found stress shadow durations typically 1-2 times longer than those predicted by the elastic model, with Calaveras Central and South segments showing shadows 4-5 times longer.

Although the traditional method used to calculate long-term loading rates in this study has been used in many previous studies, its validity has been questioned. It seems likely that the faults in

the San Francisco Bay region do not extend vertically to great depths, but that the seismogenic layer might be more like an elastic plate lying over a viscous substrate. The faults could be loaded either by displacements in this substrate, which might change in a smooth gradual fashion over the width of the region, or by stresses applied at the edges of the elastic plate. Bourne and others (1998) have suggested that the slip rates on individual faults across a fault zone can give insight as to the distribution of slip at depth, and Savage and others (1999) explored the implications of this idea for the San Francisco Bay region, although Savage (2000) subsequently suggested that in a linear system, it may not be possible to infer information about driving stresses from interseismic surface deformation. Alternatively, if the substrate had a low enough viscosity, the faults might be driven from the sides (J. Dieterich, oral communication, 2000), and each of the subparallel faults might be expected to have about the same long-term loading rate; which fault failed might then depend on stress interactions between the faults, which would tend to relax each other in large events, and relative strengths of the faults. Parsons (2001) has implemented a viscoelastic 3D finite element model driven from the sides and finds loading rates that are typically two-thirds to three-quarters of the values from elastic halfspace models used here.

Another uncertainty is whether the high level of seismicity prior to 1906 represents a normal rate for the region or a decades long pre-cursory increase in rate signaling imminent failure in a great event. This latter possibility is the subject of ongoing research (e.g., Sykes and Jaumé, 1990; Bufe and Varnes, 1993; Bowman and others, 1998). If the seismicity in the 1800's represents the "normal" rate for the Bay region, then the wearing away of the 1906 stress shadow is more ominous than if the high rates of seismicity in the 1800's were building up to the 1906 event.

Appendix R – R-factor Examples

This appendix describes several examples intended to illustrate some of the problems inherent in calculating clock changes for segments with R<1. These examples are very simple and by calculating stress changes and loading rates at the centers of locked patches they offer averaged results that don't reflect the variation in stress changes over the surface of the locked patch. Nonetheless, it is hoped that the results give some idea of the difficulties inherent in using R-factors.

In Figure R1a, a 50-km long by 10-km tall fault segment is assumed to be completely locked (R=1). Deep slip under this segment is simulated by a large vertical dislocation moving in a right-lateral sense at a long-term rate of 9-mm/yr. This configuration approximates the geometry of the Hayward South (HS) segment. A 1906-type earthquake on a parallel fault 30 km to the west induces a 3.525 bar Coulomb stress relaxation, which given the long-term loading rate at the center of the locked segment yields a 37.1 year clock delay in the time to failure of this segment.

Figure R1b shows a geometry in which the fault segment is divided into two side-by-side patches, one (L) that is locked and the second (S) that is free to slip aseismically (Table R1). It is assumed that there is no friction and no pore fluid effects acting on S. The interseismic slip on S increases the loading rate on locked patch L. Note, however, that although the long-term slip rate on the fault is assumed to be 9 mm/yr, the adjacent locked patches retard the interseismic slip on the creeping segment. For example if S is equal in area to L, the interseismic slip rate on S is 6.4 mm/yr.

When the 1906-type earthquake occurs, the loading rate on L (which is higher than the loading rate on the R=1 segment because slip on S also loads L) produces a clock delay of 32.9 years

(Table R1). Given time, however, the creeping segment S may also respond to the relaxation by slowing its rate until stresses on it again reach a steady state. The net effect of this slowdown is to enhance the relaxation on the locked patch, and for the geometry shown, the end result when a steady interseismic state is finally attained is to increase the clock delay to 37.0 years. Depending on the time to re-equilibration and the time to failure, the clock delay could presumably fall somewhere between the lower and higher value.

If all of the retarded slip in creeping segment S is ultimately released aseismically, R=0.5. But, if as seems likely, some of this catch-up slip occurs coseismically when an adjacent locked patch breaks, then R will be larger. If all of the interseismic retardation were recovered coseismically, R=0.67 in this case. Thus an important issue in deciding what R-value applies is knowing how much of the moment stored in creeping but retarded regions of the fault surface gets released coseismically rather than as postseismic afterslip.

Figure R1c shows a geometry in which the fault segment is divided into two stacked patches with the creeping patch S overlying a locked patch L. Results for this geometry are also listed in Table R1. The clock change effects for low R-values are magnified by the geometry, because in this case the center of the locked patch get closer to the deep source of the loading stress as the patch shrinks in height. Once again there is an ambiguity in R-value, depending on how much of the moment stored as retarded slip in the creeping patch gets released coseismically. There is also a time-dependent increase in the magnitude of the clock change caused by postseismic response of the creeping segment to the remote earthquake: As before, the slip rate on the creeping patch is lowered for a time by the earthquake-induced relaxation, which enhances the relaxation on the locked patch and increases the magnitude of the clock delay.

The time constant for such a response on a creeping region of a fault plane is not known. A perfectly frictionless fault would respond immediately, but even creeping faults are not "perfectly" frictionless. One way to estimate this time required for the slipping part of the fault to return to normal is to assume that the slipping part simply stops creeping in response to the relaxation and does not begin again until the equivalent slip deficit that would have been produced if that part were perfectly frictionless is made up. Table R2 lists this estimated recovery time for the various cases. These times range from 37 to 53 years, which is a relative small part of the seismic cycle (but a relatively long time to expect our elastic models to yield realistic results). Part of the southern Hayward fault stopped creeping after the 1989 Loma Prieta earthquake and resumed creep within the expected recovery time of ~ 6 years (Lienkaemper and others, 1997).

In Figure R2, the clock changes from Table R1 are shown in graphical form. The vertical arrows show the time evolution of clock changes as the creeping patch responds to the relaxing stress change. The width of the gray boxes show the range of possible R values for the given geometry depending on how much of the retarded slip gets released coseismically. The dark dashed line through the origin shows the preferred adjustment that has been applied to clock changes based on the R-factor value for a given segment. The two lighter dashed lines together with the dark dashed line are the adjustment (with weights of 0.25/0.5/0.25 respectively from top to bottom) referred to previously. The adjustment using the single dark dashed line was preferred for its simplicity, and because the stacked examples seemed more likely to simulate real fault behavior, with large earthquakes nucleating at greater rather than shallower depth. The results were not very different regardless of adjustment method chosen.

The bottom line is that when it comes to calculating clock changes, the assumed geometry of locked and slipping regions can make a big difference even for identical R-factors. There could

also be a time evolution to the clock change, as patches free to slip respond to coseismic stress changes. Finally, the amount of moment tied up in retarded slip on creeping parts of the fault can represent a substantial fraction of the total stored moment (Table R3), and the amount of this moment that gets released coseismically affects not only the R-factor, but the magnitude of earthquakes on that fault segment, and hence the hazard.

Appendix LP – 1989 Loma Prieta Earthquake and Segments SAS and SAP

Because WG99's Santa Cruz Mountains (SAS) and Peninsula (SAP) segments of the San Andreas fault system lie so close to the Loma Prieta rupture surface, the approach used to estimate clock changes after 1906 could not be used. Regardless of rupture model used, the variations in Coulomb stress change over the surface of these segments was so great that using the center of the segment as the sampling point failed to capture the range of values (Figure 1).

An alternate approach, suggested by Bill Ellsworth, subdivided the SAS and SAP segments into 2-km by 2-km patches under the trace of the San Andreas fault. The median value and the range of values of Coulomb stress change were then calculated for depths between 6-km and 20-km on two subregions of these segments most likely to have been affected by the 1989 earthquake and/or deemed most likely to nucleate future earthquakes. For SAS, this segment consisted of the northernmost 40 km and for SAP the southernmost 20 km.

The three 1989 rupture models used were those of Arnadottir and Segall (1994) based on inversions of geodetic information, Beroza (1995) based on inversion of strong motion data, and Wald and Heaton (1995) based on teleseismic and strong motion records. As can be seen from Figure LP1, there are considerable variations in detail in the calculated shear stress changes produced by these model ruptures on the San Andreas fault surface, although in general, the upper 6 km along the length of the rupture in the adjacent SAS segment tends to be more stressed while the region below 6 km tends to be relaxed. It seems unlikely that the upper 6 km could host a future earthquake of M>6.7, although the region below might well be capable. The remaining ~12 km at the south end of the SAS segment is adjacent to the creeping section of the San Andreas fault lying south of San Juan Bautista, and also seemed less likely to nucleate a M>6.7 earthquake.

For the southern end of the SAP segment, all models indicate increased stress above about 10 km and patches of decreased stress below. If we knew where the next large earthquake on the SAP segment was likely to nucleate, we would have a better idea of the likely impact of 1989 on the SAP segment, but in the absence of such knowledge, the best we can do is assign a large uncertainty to the clock change values—in this case both positive and negative bounds.

As in the 1906 calculation, weighted values of friction and pore parameters shown in Table 1 were used in a Monte Carlo process to estimate the average coseismic Coulomb stress changes shown in Table LP1. The three rupture models were given equal weight, so these values were averaged, as were the 90% confidence bounds, and the resulting average of averages were divided by the median loading rates for these segments to yield estimates of clock changes.

The results shown in Table LP1 with very large confidence bounds of both positive and negative signs are consistent with our lack of knowledge about the processes at work on these segments and about the critical regions for earthquake nucleation.

References Cited

Arnadottir, T., and Segall, P., 1994, The 1989 Loma Prieta earthquake imaged from inversion of geodetic data: Journal of Geophysical Research, v. 99, p. 21,835-21,855.

Bakun, W.H., 1999, Seismic activity of the San Francisco Bay region: Seismological Society of America Bulletin, v. 89, p. 764-784.

Beeler, N.M., Simpson, R.W., Hickman, S.H., and Lockner, D.A., 2000, Pore fluid pressure, apparent friction, and Coulomb failure: Journal of Geophysical Research, v. 105, p. 25,533-25,542.

Beroza, G.C., 1995, Rupture history of the earthquake from high-frequency strong-motion data, in, Spudich, P., ed., The Loma Prieta earthquake of October 17, 1989—Mainshock characteristics: U.S. Geological Survey Professional Paper 1550-A, p. A9-A32.

Bourne, S.J., England, P.C., and Parsons, B., 1998, The motion of crustal blocks driven by flow of the lower lithosphere: Implications for slip rates of faults in the South Island of New Zealand and southern California: Nature, v. 391, p. 655-659.

Bowman, D.D., 1998, An observational test of the critical earthquake concept: Journal of Geophysical Research, v. 103, p. 24,359-24,372.

Bufe, C.G., and Varnes, D.J., 1993, Predictive modeling of the seismic cycle of the greater San Francisco Bay region: Journal of Geophysical Research, v. 98, p. 9871-9883.

Dieterich, J., 1994, A constitutive law for rate of earthquake production and its application to earthquake clustering: Journal of Geophysical Research, v. 99, p. 2601-2618.

Dieterich, J., Cayol, V., and Okubo, P., 2000, The use of earthquake rate changes as a stress meter at Kilauea volcano: Nature, v. 408, p. 457-460.

Deng, J., and Sykes, L.R., 1997, Evolution of the stress field in southern California and triggering of moderate-size earthquakes: A 200-year perspective: Journal of Geophysical Research, v. 102, p. 9859-9886.

Ellsworth, W.L., Lindh, A.G., Prescott, W.H., and Herd, D.G., 1981, The 1906 San Francisco earthquake and the seismic cycle, *in* Simpson, D.W., and Richards, P.G., eds., Earthquake prediction; an international review (Maurice Ewing series 4): Washington, D.C., American Geophysical Union, p. 126-140.

Geist, E.L., and Andrews, D.J., 2000, Slip rates on San Francisco Bay area faults from anelastic deformation of the continental lithosphere: Journal of Geophysical Research, v. 105, p. 25,543-25,552.

Gomberg, J., Beeler, N.M., Blanpied, M.L., and Bodin, P., 1998, Earthquake triggering by transient and static deformations: Journal of Geophysical Research, v. 103, p. 24,411-24,426.

Gomberg, J., Beeler, N., and Blanpied, M., 2000, On rate-state and Coulomb failure models: Journal of Geophysical Research, v. 105, p. 7857-7871.

Harris, R.A., 1998, Introduction to special section: Stress triggers, stress shadows, and implications for seismic hazard: Journal of Geophysical Research, v. 103, p. 24,347-24,358.

Harris, R.A., and Simpson, R.W., 1998, Suppression of large earthquakes by stress shadows: A comparison of Coulomb and rate-and-state failure: Journal of Geophysical Research, v. 103, p. 24,439-24,451.

Jaeger, J.C., and Cook, N.G.W., 1979, Fundamentals of rock mechanics (3rd ed.): London, Chapman and Hall, 593 p.

Jaumé, S.C., and Sykes, L.R., 1992, Changes in state of stress on the southern San Andreas fault resulting from the California earthquake sequence of April to June, 1992: Science, v. 258, p. 1325-1328.

Jaumé, S.C., and Sykes, L.R., 1996, Evolution of moderate seismicity in the San Francisco Bay region, 1850 to 1993: Seismicity changes related to the occurrence of large and great earthquakes: Journal of Geophysical Research, v. 101, p. 765-789.

Kenner, Shelley, and Segall, Paul, 1999, Time dependence of the stress-shadowing effect and its relation to the structure of the lower crust: Geology, v. 27, n. 2, p. 119-122.

Kenner, Shelley, and Segall, Paul, 2000, Postseismic deformation following the 1906 San Francisco earthquake: Journal of Geophysical Research, v. 105, p. 13,195-13,209.

Kilb, D., Gomberg, J., Bodin, P., 2000, Triggering of earthquake aftershocks by dynamic stresses: Nature, v. 408, p. 570-574.

Lienkaemper, J.J., Borchardt, G., and Lisowski, M., 1991, Historic creep rate and potential for seismic slip along the Hayward fault, California: Journal of Geophysical Research, v. 96, p. 18,261-18,283.

Lienkaemper, J.J., Galehouse, J.S., and Simpson, R.W., 1997, Creep response of the Hayward fault to stress changes caused by the Loma Prieta earthquake: Science, v. 276, p. 2014-2016.

Linker, M.F., and Rice, J.R., 1997, Models of postseismic deformation and stress transfer associated with the Loma Prieta earthquake, in Reasenberg, P.A., ed., The Loma Prieta, California, earthquake of October 17, 1989—aftershocks and postseismic effects: U.S. Geological Survey Professional Paper 1550D, p. 253-275.

Okada, Y., 1992, Internal deformation due to shear and tensile faults in a half-space: Seismological Society of America Bulletin, v. 82, no. 2, p. 1018-1040.

Parsons, Tom, Stein, R.S., Simpson, R.W., Reasenberg, P.A., 1999, Stress sensitivity of fault seismicity; a comparison between limited-offset oblique and major strike-slip faults: Journal of Geophysical Research, v. 104, p. 20,183-20,202.

Parsons, Tom, Toda, Shinji, Stein, R.S., Barka, Aykut, Dieterich, J.H., 2000, Heightened odds of large earthquakes near Istanbul; an interaction-based probability calculation: Science, v. 288, p. 661-665.

Parsons, Tom, 2001, Post-1906 stress recovery of the San Andreas fault system calculated from 3-D finite element analysis: (submitted to JGR).

Pollitz, F.F, Burgmann, Roland, and Segall, Paul, 1998, Joint estimation of afterslip rate and postseismic relaxation following the 1989 Loma Prieta earthquake: Journal of Geophysical Research, v. 103, n. B11, p. 26975-26922.

Reasenberg, P.A., and Simpson, R.W., 1992, Response of regional seismicity to the static stress change produced by the Loma Prieta earthquake: Science, v. 255, no. 5052, p. 1687-1690.

Rice, J.R., Cocco, Massimo, 2000, Pore pressure transitions in Coulomb stress analysis of earthquake interactions: Eos, Transactions, American Geophysical Union, v. 81, p. F1086.

Roeloffs, E., 1996, Poroelastic techniques in the study of earthquake related hydrologic phenomena: Adv. Geophys., v. 37, p. 135-195.

Savage, J.C., and Lisowski, M., 1993, Inferred depth of creep on the Hayward fault, Central California: Journal of Geophysical Research, v. 98, p. 787-793.

Savage, J.C., Svarc, J.L., Prescott, W.H., 1999, Geodetic estimates of fault slip rates in the San Francisco Bay area: Journal of Geophysical Research, v. 104, p. 4995-5002.

Savage, J.C., 2000, Viscoelastic-coupling model for the earthquake cycle driven from below: Journal of Geophysical Research, v. 105, p. 25,525-25,532.

Scholz, C.H., 1990, The mechanics of earthquakes and faulting: Cambridge, U.K., Cambridge University Press, 439 p.

Simpson, R.W., and Reasenberg, P.A., 1994, Earthquake induced static stress changes on central California faults, in, Simpson, R.W., ed., The Loma Prieta earthquake of October 17, 1989—tectonic processes and models: U.S. Geological Survey Professional Paper 1550-F, p. 55-89.

Simpson, R.W., Lienkaemper, J.J., and Galehouse, J.S., 2001, Variations in creep rate along the Hayward fault, California, interpreted as changes in depth of creep: Geophysical Research Letters, v. 28, p. 2269-2272.

Stein, R.S., Barka, A.A., and Dieterich, J.H., 1997, Progressive failure on the North Anatolian fault since 1939 by earthquake stress triggering: Geophysical Journal International, v. 128, p. 594-604.

Sykes, L.R., and Jaumé, S., 1990, Seismic activity on neighboring faults as a long-term precursor to large earthquakes in the San Francisco Bay area: Nature, v. 348, p. 595-599.

Thatcher, W., Marshall, G., and Lisowski, M., 1997, Resolution of fault slip along the 470-km-long rupture of the great 1906 San Francisco earthquake and its implications: Journal of Geophysical Research, v. 102, p. 5353-5367.

Toda, Shinji, Stein, R.S., Reasenberg, P.A., and Dieterich, J.H., 1998, Stress transferred by the 1995 Mw=6.9 Kobe, Japan, shock: Effect on aftershocks and future earthquake probabilities: Journal of Geophysical Research, v. 103, p. 24,543-24,565.

Toda, Shinji, and Stein, R.S., 2001, Response of the San Andreas fault to the 1983 Coalinga-Nunez earthquakes: A test of interaction-induce probability changes at Parkfield: Journal of Geophysical Research, (submitted).

Wald, D.J., and Heaton, T.H., 1995, Strong-motion and broadband teleseismic analysis of the earthquake for rupture process and hazards assessment, in, Spudich, P., ed., The Loma Prieta earthquake of October 17, 1989—Mainshock characteristics: U.S. Geological Survey Professional Paper 1550-A, p. A235-A262.

Ward, S.N., 2000, San Francisco Bay area earthquake simulations: A step toward a standard physical earthquake model: Bulletin of the Seismological Society of America, v. 90, p. 370-386.

Zoback, M.D., Zoback, M.L., Mount, V.S., Suppe, John, Eaton, J.P., Healy, J.H., Oppenheimer, D.H., Reasenberg, P.A., Jones, L.M., Raleigh, C.B., Wong, I.G., Scotti, Oona, and Wentworth, C.M., 1987, New evidence on the state of stress of the San Andreas fault system: Science, v. 238, no. 4830, p. 1105-1111.

Figure Captions

Figure 1. Regional stress relaxation shadow produced by the 1906 earthquake. Colors represent decreased (blue) or increased (red) right-lateral shear stress caused by the 1906 event at 6.5 km depth on vertical N35W striking planes. The red line, hachured at 10 km intervals, represents the 1906 rupture model of Thatcher and others (1997) with their preferred offsets in meters printed next to each segment. The black lines, terminated by circles are WG99 fault segments. The red region to the southeast of the 1906 rupture contains the creeping section of the San Andreas fault (not shown).

Figure 2. Coulomb stress evolution diagram for a typical Bay region fault segment showing how a 1906-induced relaxation of the segment would delay its time to failure in a Coulomb failure model. The original failure time $\mathbf{t_A}$ gets delayed until $\mathbf{t_B}$ yielding the clock change shown. The upward slope of the Coulomb stress level curve between earthquakes represents the long-term loading on the fault segment by plate tectonic forces. The gray region indicates the time during which the fault lies in the 1906 stress shadow; the parallelogram rising from the top of the shadow region up to the failure threshold line indicates that the duration of the shadow is identical to the clock change.

Figure R1. Three geometric configurations used in R-factor examples. (a) A locked 50-km long segment, lying between two semi-infinite locked segments, loaded by 9 mm/yr of slip at depth. (b) The segment is subdivided into two side-by-side parts, one slipping freely (S) and the other completely locked (L). (c) The segment is divided into a slipping part (S) lying above a locked part (L). Gray shaded regions are creeping continuously. Results for different relative widths and heights are given in Table R1.

Figure R2. Clock changes estimated from the examples in Table R1 for the geometry where the slipping part of the fault is next (N) to the locked part as in Figure R1b, or over (O) the locked part as in Figure R1c. Subscripts to N and O are the fraction of segment area that is locked.

Black filled squares are clock changes before the slipping segment has had a chance to relax. White filled squares are same after slipping segment has responded fully to the relaxing stress changes. Grey rectangles represent range of clock changes and R-factors depending on how much triggered slip has occurred on the freely slipping part and how much of the retarded slip in slipping areas is released coseismically.

Figure LP1. Horizontal shear stress changes on SAS and SAP segments of the San Andreas fault calculated using three rupture models for the 1989 Loma Prieta earthquake: (a) Arnadottir and Segall (1994), (b) Beroza (1995), (c) Wald and Heaton (1995). The rectangular patches making up these segments are 2-km by 2-km in size and extend from sea level to 20-km depth. Other WG99 fault segments are indicated by red lines and terminated by red dots.

Table 1. – Weights and Choices Entering into Monte Carlo Generation of Instances

Parameter Type	Choices	Weights	Comments	References
Pore fluid effects	Yes / no	0.5 / 0.5	Importance of pore fluid effects is poorly understood.	Beeler and others (2000), Rice and Cocco (2000).
Pore fluid models	"Rice" / "isotropic - poroelastic"	0.5 / 0.5	Applicable model is not known. (B = 1 for both models.)	Beeler and others (2000), Rice and Cocco (2000).
Coefficient of friction	0.0 / 0.4 / 0.8	0.5 / 0.25 / 0.25	Some evidence indicates that the major strike-slip faults act like low-friction faults.	Zoback et al. (1987) Reasenberg and Simpson (1992), Parsons and others (1999).
1906 Rupture depth	10 km / 15 km	0.5 / 0.5	Depth is poorly controlled. Larger depth allows for afterslip also.	Thatcher and others (1997).
1906 Slip distribution	Preferred / min / max	0.6 / 0.2 / 0.2	Takes account of uncertainties in Thatcher et al. slip model.	Thatcher and others (1997).
1989 Rupture models	Arnadottir / Beroza / Wald	0.33 / 0.33 / 0.33	Models produce different results in detail on closer segments.	Arnadottir and Segall (1994), Beroza (1995), Wald and Heaton (1995).

Table 2. 1906 Clock Changes, Coseismic Coulomb Stress Changes, and Long-Term Loading Rates

Seg-ment Num-ber	**Median Clock Change (years)**	Lower 90% Con-fidence Bound (years)	Upper 90% Con-fidence Bound (years)	**Median Co-seismic Stress Change (bars)**	Lower 90% Con-fidence Bound (bars)	Upper 90% Con-fidence Bound (bars)	**Median Loading Rate (bars/yr)**	Lower 90% Con-fidence Bound (bars/yr)	Upper 90% Con-fidence Bound (bars/yr)	Segment Code and Name	
1*	-133.0	-437.5	-13.7	-24.35	-77.27	-2.71	0.171	0.138	0.197	SAS	SAF Santa Cruz
2*	-172.9	-337.4	-61.1	-32.05	-56.71	-11.82	0.187	0.151	0.223	SAP	SAF Peninsula
3*	-212.7	-639.6	75.1	-63.25	-176.16	20.41	0.283	0.226	0.345	SAN	SAF North Coast
4*	-87.9	-223.7	-16.5	-24.33	-60.44	-4.80	0.280	0.223	0.341	SAO	SAF Offshore
5	**-13.5**	-33.0	-0.1	**-3.10**	-7.34	-0.03	**0.138**	0.113	0.164	HS	Hayward South
6	**-25.4**	-44.0	-13.2	**-5.76**	-8.66	-3.27	**0.131**	0.108	0.155	HN	Hayward North
7	**-27.6**	-58.4	-5.2	**-3.36**	-7.13	-0.64	**0.121**	0.098	0.140	RC	Rodgers Creek
8	**-2.3**	-10.5	0.0	**-3.30**	-11.49	-0.91	**0.262**	0.208	0.339	CS	Calaveras South
9	**-4.0**	-14.0	-0.4	**-3.90**	-8.96	-0.39	**0.202**	0.173	0.243	CC	Calaveras Central
10	**-15.1**	-33.4	-2.8	**-2.41**	-4.80	-0.43	**0.124**	0.102	0.148	CN	Calaveras North
11	**-16.3**	-36.8	-4.9	**-2.28**	-3.56	-1.32	**0.066**	0.045	0.083	CON	Concord
12	**-9.7**	-30.1	-2.2	**-1.43**	-3.44	-0.35	**0.069**	0.037	0.086	GVS	Green Valley South
13	**-4.7**	-18.8	0.3	**-0.84**	-2.40	0.06	**0.085**	0.042	0.136	GVN	Green Valley North
14	**-6.2**	-17.8	14.3	**-0.24**	-0.48	0.37	**0.034**	0.013	0.042	SGS	San Gregorio South
15	**-55.1**	-136.6	-6.7	**-6.39**	-16.75	-0.80	**0.106**	0.077	0.129	SGN	San Gregorio North
16	**-19.0**	-38.1	-7.6	**-1.07**	-2.10	-0.39	**0.049**	0.038	0.061	GS	Greenville South
17	**-28.9**	-67.7	-11.5	**-1.27**	-2.02	-0.47	**0.037**	0.021	0.049	GN	Greenville North
18	**-1.6**	-4.4	5.5	**-0.09**	-0.16	0.32	**0.057**	0.023	0.091	MTD	Mount Diablo

Confidence bounds are relative to the models used, rather than absolute (see text).

Negative values for clock changes indicate a delay. Negative values for coseismic Coulomb stress changes indicate a relaxation; that is, the segment moves farther from failure.

Clock changes for starred (*) San Andreas fault segments are not used in the probability calculations, because probabilities for these segments are governed by the date of the last event, which is known at 1906.

Table 3. – 1906 Clock Changes: Comparison with Prior Results

Segment Number	Median 1906 Clock Change (yr) using wts with one R-factor applied to dT	[1] "Simple" 1906 Clock Change (yr) from Open-File Report 99-517	WG99 Seismogenic Scaling Factor (R-factor)	Segment Code and Name	
1	**-133.0**	-	0.8/0.9/1.0	SAS	SAF Santa Cruz
2	**-172.9**	-	0.9/1.0/1.0	SAP	SAF Peninsula
3	**-212.7**	-	0.9/1.0/1.0	SAN	SAF North Coast
4	**-87.9**	-	0.9/1.0/1.0	SAO	SAF Offshore
5	**-13.5**	-20.1	0.4/0.6/0.8	HS	Hayward South
6	**-25.4**	-31.1	0.4/0.6/0.8	HN	Hayward North
7	**-27.6**	-27.9	0.9/1.0/1.0	RC	Rodgers Creek
8	**-2.3**	-13.7	0.0/0.2/0.4	CS	Calaveras South
9	**-4.0**	-13.8	0.3/0.5/0.7	CC	Calaveras Central
10	**-15.1**	-14.6	0.7/0.8/0.9	CN	Calaveras North
11	**-16.3**	-21.2	0.2/0.5/0.8	CON	Concord
12	**-9.7**	-13.1	0.2/0.5/0.8	GVS	Green Valley South
13	**-4.7**	-8.7	0.2/0.5/0.8	GVN	Green Valley North
14	**-6.2**	-5.8	0.8/0.9/1.0	SGS	San Gregorio South
15	**-55.1**	-42.4	0.8/0.9/1.0	SGN	San Gregorio North
16	**-19.0**	-15.8	0.8/0.9/1.0	GS	Greenville South
17	**-28.9**	-23.1	0.8/0.9/1.0	GN	Greenville North
18	**-1.6**	-1.3	1.0/1.0/1.0	MTD	Mount Diablo

[1] The "simple" clock change from WG99 (1999) was the result obtained from the use of preferred parameters and geometries (zero coefficient of friction, no pore fluids, 10-km deep 1906 rupture, Thatcher and others (1997) preferred slip), rather than a weighted combination of parameters and geometries. No adjustment for R-factor was applied.

Table 4. 1989 Clock Changes, Coseismic Coulomb Stress Changes, and Long-Term Loading Rates

Seg-ment Num-ber	**Median Clock Change (years)**	Lower 90% Con-fidence Bound (years)	Upper 90% Con-fidence Bound (years)	**Median Co-seismic Stress Change (bars)**	Lower 90% Con-fidence Bound (bars)	Upper 90% Con-fidence Bound (bars)	**Median Loading Rate (bars/yr)**	Lower 90% Con-fidence Bound (bars/yr)	Upper 90% Con-fidence Bound (bars/yr)	Segment Code and Name	
1*	(-23.5)	(-970.4)	329.7	-4.38	-193.25	59.47	0.170	0.138	0.197	SAS	SAF Santa Cruz
2*	(1.3)	(0.7)	(3.0)	0.25	0.13	0.54	0.187	0.151	0.223	SAP	SAF Peninsula
3	**0.0**	0.0	0.0	**0.01**	0.00	0.01	**0.283**	0.227	0.345	SAN	SAF North Coast
4	**0.0**	0.0	0.0	**0.00**	0.00	0.00	**0.280**	0.223	0.341	SAO	SAF Offshore
5	**-1.0**	-2.3	-0.4	**-0.23**	-0.52	-0.10	**0.138**	0.113	0.164	HS	Hayward South
6	**-0.0**	-0.2	0.0	**-0.01**	-0.05	0.00	**0.131**	0.108	0.155	HN	Hayward North
7	**0.0**	-0.1	0.0	**0.00**	-0.01	0.00	**0.121**	0.098	0.140	RC	Rodgers Creek
8	**-0.3**	-1.2	0.0	**-0.52**	-1.18	-0.04	**0.262**	0.207	0.336	CS	Calaveras South
9	**-0.0**	-0.7	2.2	**-0.01**	-0.51	1.70	**0.202**	0.173	0.243	CC	Calaveras Central
10	**-1.7**	-3.4	-0.9	**-0.26**	-0.51	-0.14	**0.124**	0.102	0.148	CN	Calaveras North
11	**-0.4**	-1.0	-0.1	**-0.05**	-0.10	-0.03	**0.066**	0.046	0.083	CON	Concord
12	**0.0**	-0.2	0.1	**0.01**	-0.03	0.01	**0.069**	0.036	0.086	GVS	Green Valley South
13	**0.0**	-0.1	0.1	**0.01**	-0.02	0.01	**0.085**	0.042	0.137	GVN	Green Valley North
14	**-6.2**	-17.2	1.3	**-0.24**	-0.35	0.04	**0.034**	0.013	0.042	SGS	San Gregorio South
15	**-1.8**	-9.6	0.3	**-0.21**	-1.08	0.04	**0.106**	0.077	0.129	SGN	San Gregorio North
16	**-4.7**	-7.3	1.2	**-0.26**	-0.36	0.06	**0.049**	0.038	0.061	GS	Greenville South
17	**-4.4**	-7.8	-1.6	**-0.18**	-0.27	-0.06	**0.037**	0.021	0.049	GN	Greenville North
18	**-1.2**	-3.2	-0.5	**-0.07**	-0.13	-0.03	**0.057**	0.023	0.090	MTD	Mount Diablo

Confidence bounds are relative to the models used, rather than absolute (see text).

Negative values for clock changes indicate a delay. Negative values for coseismic Coulomb stress changes indicate a relaxation; that is, the segment moves farther from failure.

Clock changes for starred (*) San Andreas fault segments (SAS and SAP) were replaced by values from more detailed models for use in the probability calculations. (See text for details.)

Table 5. – 1989 Clock Changes: Preferred Values and Comparison with Prior Values

Segment Number	**Preferred Median Clock Change (years)**	Lower 90% Confidence Bound (years)	Upper 90% Confidence Bound (years)	**Prior 1989 Clock Change (yr) from Open-File Report 99-517**	Segment Code and Name	
1*	**-66.8**	-229.0	+127.3	-60	SAS	SAF Santa Cruz
2*	**-0.5**	-48.7	+19.2	+5	SAP	SAF Peninsula
3	**0.0**	0.0	0.0	-	SAN	SAF North Coast
4	**0.0**	0.0	0.0	-	SAO	SAF Offshore
5	**-1.0**	-2.3	-0.4	-	HS	Hayward South
6	**-0.0**	-0.2	0.0	-	HN	Hayward North
7	**0.0**	-0.1	0.0	-	RC	Rodgers Creek
8	**-0.3**	-1.2	0.0	-	CS	Calaveras South
9	**-0.0**	-0.7	2.2	-	CC	Calaveras Central
10	**-1.7**	-3.4	-0.9	-	CN	Calaveras North
11	**-0.4**	-1.0	-0.1	-	CON	Concord
12	**0.0**	-0.2	0.1	-	GVS	Green Valley South
13	**0.0**	-0.1	0.1	-	GVN	Green Valley North
14	**-6.2**	-17.2	1.3	-	SGS	San Gregorio South
15	**-1.8**	-9.6	0.3	-	SGN	San Gregorio North
16	**-4.7**	-7.3	1.2	-	GS	Greenville South
17	**-4.4**	-7.8	-1.6	-	GN	Greenville North
18	**-1.2**	-3.2	-0.5	-	MTD	Mount Diablo

The values for starred (*) segments (SAS andSAP) were obtained using more detailed models as described in the text and appendix LP.

Table 6 - Revised Clock Change Values for 1906 and 1989 Earthquakes

	1906			1989				
Seg-ment Num-ber	**Median Clock Change (years)**	Lower 90% Con-fidence Bound (years)	Upper 90% Con-fidence Bound (years)	**Median Clock Change (years)**	Lower 90% Con-fidence Bound (years)	Upper 90% Con-fidence Bound (years)	Segment Code and Name	
1	–	–	–	**-66.8**	-229.0	+127.3	SAS	SAF Santa Cruz
2	–	–	–	**-0.5**	-48.7	+19.2	SAP	SAF Peninsula
3	–	–	–	**0.0**	0.0	0.0	SAN	SAF North Coast
4	–	–	–	**0.0**	0.0	0.0	SAO	SAF Offshore
5	**-13.5**	-33.0	-0.1	**-1.0**	-2.3	-0.4	HS	Hayward South
6	**-25.4**	-44.0	-13.2	**-0.0**	-0.2	0.0	HN	Hayward North
7	**-27.6**	-58.4	-5.2	**0.0**	-0.1	0.0	RC	Rodgers Creek
8	**-2.3**	-10.5	0.0	**-0.3**	-1.2	0.0	CS	Calaveras South
9	**-4.0**	-14.0	-0.4	**-0.0**	-0.7	2.2	CC	Calaveras Central
10	**-15.1**	-33.4	-2.8	**-1.7**	-3.4	-0.9	CN	Calaveras North
11	**-16.3**	-36.8	-4.9	**-0.4**	-1.0	-0.1	CON	Concord
12	**-9.7**	-30.1	-2.2	**0.0**	-0.2	0.1	GVS	Green Valley South
13	**-4.7**	-18.8	0.3	**0.0**	-0.1	0.1	GVN	Green Valley North
14	**-6.2**	-17.8	14.3	**-6.2**	-17.2	1.3	SGS	San Gregorio South
15	**-55.1**	-136.6	-6.7	**-1.8**	-9.6	0.3	SGN	San Gregorio North
16	**-19.0**	-38.1	-7.6	**-4.7**	-7.3	1.2	GS	Greenville South
17	**-28.9**	-67.7	-11.5	**-4.4**	-7.8	-1.6	GN	Greenville North
18	**-1.6**	-4.4	5.5	**-1.2**	-3.2	-0.5	MTD	Mount Diablo

(Negative values for clock changes indicate a delay.)

Table R1 – Summary of R-factor Example Results

Geometry	Fraction of Area Locked L/(L+S)	Long-Term Loading at Center of L with slip on S (bar/yr)	Coseismic Stress Change at Center of L right after event (bar)	Coseismic Stress Change at Center of L with afterslip on S (bar)	Inter-seismic slip rate on S (mm/yr)	Clock Change right after event (years)	Clock Change with afterslip on S (years)	R-factor (assuming all moment accumulated interseismically in retarded slip on S gets released coseismically)	R-factor (assuming all moment accumulated interseismically in retarded slip on S gets released aseismically)
S next to L	1.00	0.095	-3.525	-	-	-37.1	-	1.00	1.00
"	0.75	0.098	"	-3.629	4.2	-36.0	-37.0	0.88	0.75
"	0.50	0.107	"	-3.956	6.4	-32.9	-37.0	0.67	0.50
"	0.25	0.138	"	-5.115	7.4	-25.6	-37.1	0.38	0.25
"	0.10	0.252	"	-9.367	7.8	-14.0	-37.2	0.22	0.10
S over L	1.00	0.095	-3.525	-	-	-37.1	-	1.00	1.00
"	0.75	0.098	-3.346	-3.858	1.7	-30.4	-26.3	0.95	0.75
"	0.50	0.107	-3.139	-5.212	3.5	-15.3	-25.4	0.83	0.50
"	0.25	0.138	-2.910	-9.770	5.5	-6.3	-21.2	0.54	0.25
"	0.10	0.252	-2.764	-23.777	6.9	-2.2	-18.9	0.31	0.10

S is a rectangular area of a fault segment free to slip aseismically; L is a rectangular locked area that fails only in earthquakes. The two rectangles fill a fault segment that is 50 km long and 10 km tall, either side by side with S next to L, or stacked with S over L.

Deep long-term slip rate is assumed to be at 9 mm/yr.

Coseismic event is on a 400 km long, 10 km tall parallel fault surface 30 km away, which slips by 4 m right-laterally in the event.

Table R2 – More R-factor Example Results

Geometry	Fraction of Area Locked L/(L+S)	Inter-seismic slip rate on S (mm/yr)	Fraction of total stored moment in slipping region S	Magnitude equivalent of total stored moment per century	Slip equivalent to relaxation stress applied to S (mm/yr)	Estimated recovery time = slip equivalent/ interseismic slip rate (years)	R-factor (assuming all moment accumulated interseismically in retarded slip on B gets released coseismically)	R-factor (assuming all moment accumulated interseismically in retarded slip on B gets released aseismically)
S next to L	1.00	-	0.0	6.8	-	-	1.00	1.00
"	0.75	4.2	0.15	6.7	156	37	0.88	0.75
"	0.50	6.4	0.22	6.6	237	37	0.67	0.50
"	0.25	7.4	0.35	6.5	275	37	0.38	0.25
"	0.10	7.8	0.55	6.3	288	37	0.22	0.10
S over L	1.00	-	0.0	6.8	-	-	1.00	1.00
"	0.75	1.7	0.21	6.7	090	53	0.95	0.75
"	0.50	3.5	0.38	6.7	172	50	0.83	0.50
"	0.25	5.5	0.54	6.6	241	44	0.54	0.25
"	0.10	6.9	0.68	6.4	275	40	0.31	0.10

S is a rectangular area of a fault segment free to slip aseismically; L is a rectangular locked area that fails only in earthquakes. The two rectangles fill a fault segment that is 50 km long and 10 km tall, either side by side with S next to L, or stacked with S over L.

Deep long-term slip rate is assumed to be at 9 mm/yr.

Coseismic event is on a 400 km long, 10 km tall parallel fault surface 30 km away, which slips by 4 m right-laterally in the event.

Table LP1 – Estimated Clock Changes for SAS and SAP from Three 1989 Rupture Models

	SAS – north 40 km			**SAP – south 20 km**		
	Average coseismic Coulomb stress change (bars)	Lower 90% confidence stress change (bars)	Upper 90% confidence stress change (bars)	Average coseismic Coulomb stress change (bars)	Lower 90% confidence stress change (bars)	Upper 90% confidence stress change (bars)
Arnodottir	-12.6	-70.9	+14.2	-0.6	-20.3	+7.3
Beroza	-11.0	-56.8	+26.7	0.2	-1.2	+1.0
Wald	-9.6	-43.1	+26.1	-0.1	-6.7	+2.9
Average	**-11.1**	**-40.3**	**+22.4**	**-0.1**	**-9.4**	**+3.7**
Median Loading Rate (bars/yr)	0.176 bar/yr			0.193 bar/yr		
Estimated Clock Change (yrs)	**-66.8 yr**	**-229.0 yr**	**+127.3 yr**	**-0.5 yr**	**-48.7 yr**	**+19.2 yr**

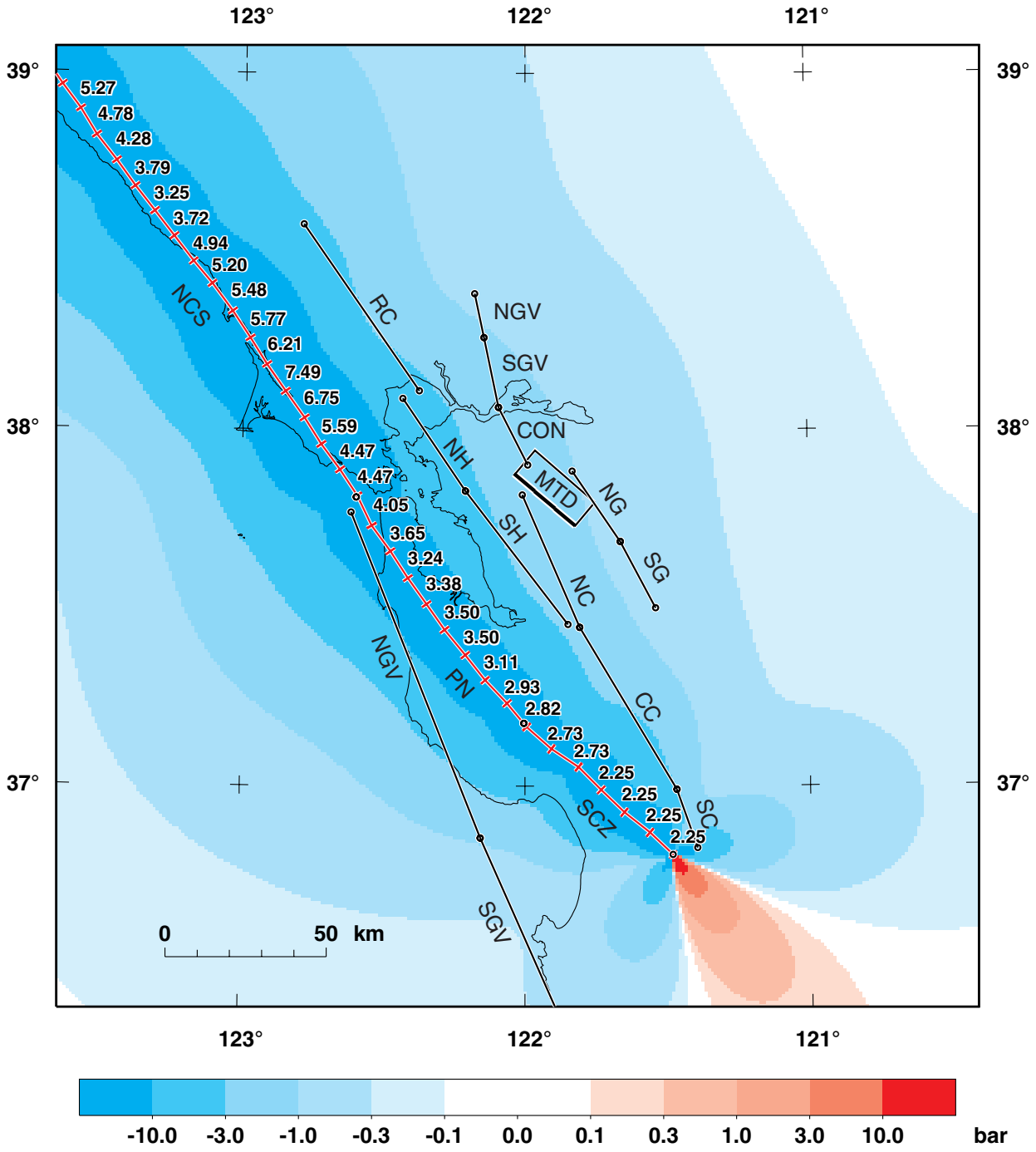
123°
122°
121°
39°
38°
37°
5.27
4.78
4.28
3.79
3.25
3.72
4.94
5.20
5.48
5.77
6.21
7.49
6.75
5.59
4.47
4.47
4.05
3.65
3.24
3.38
3.50
3.50
3.11
2.93
2.82
2.73
2.73
2.25
2.25
2.25
2.25
NCS
RC
NGV
SGV
CON
MTD
NH
SH
NG
SG
NC
CC
SC
SCZ
PN
NGV
SGV
0
50 km
-10.0
-3.0
-1.0
-0.3
-0.1
0.0
0.1
0.3
1.0
3.0
10.0
bar

Figure 1

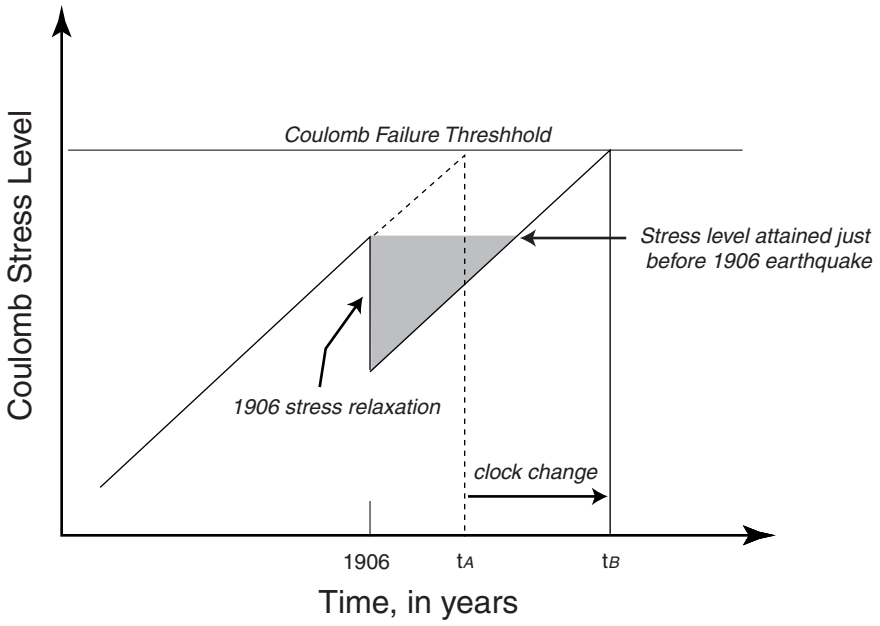
Coulomb Stress Level
Coulomb Failure Threshhold
Stress level attained just
before 1906 earthquake
1906 stress relaxation
clock change
1906
tA
tB
Time, in years

Figure 2

(a)

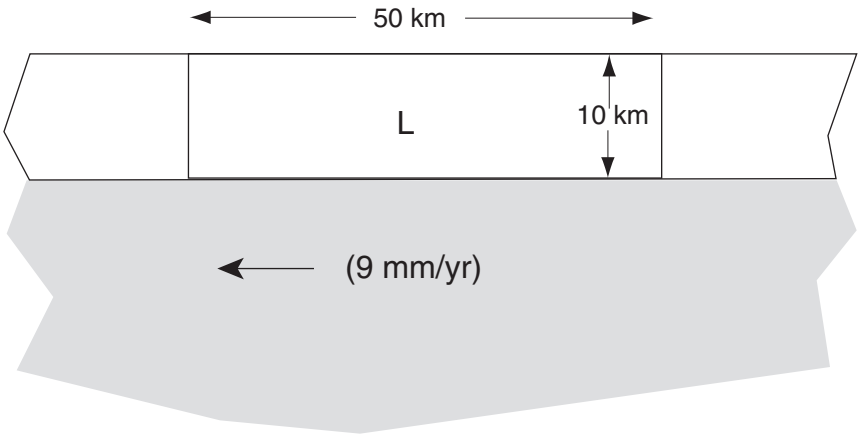

(b)

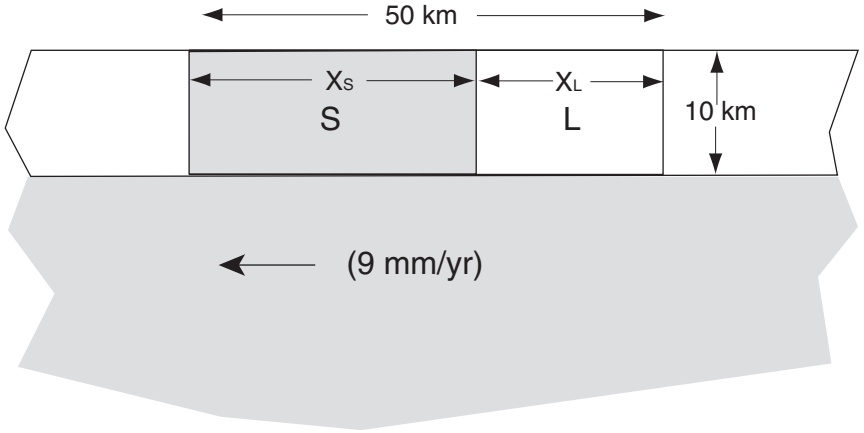

(c)

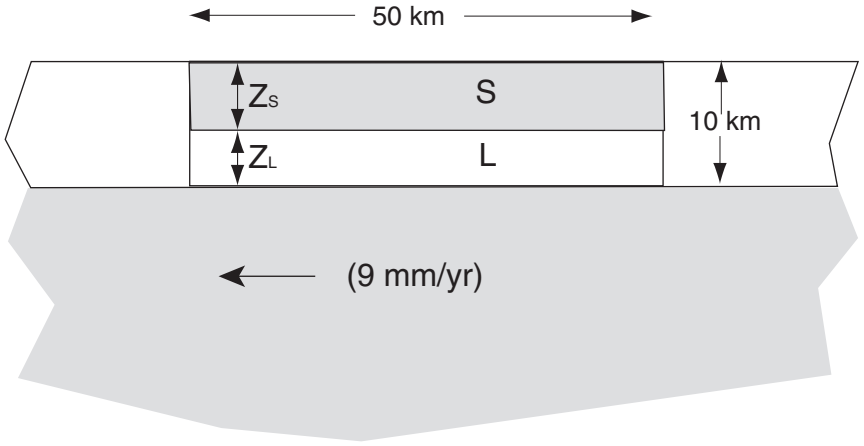

Figure R1

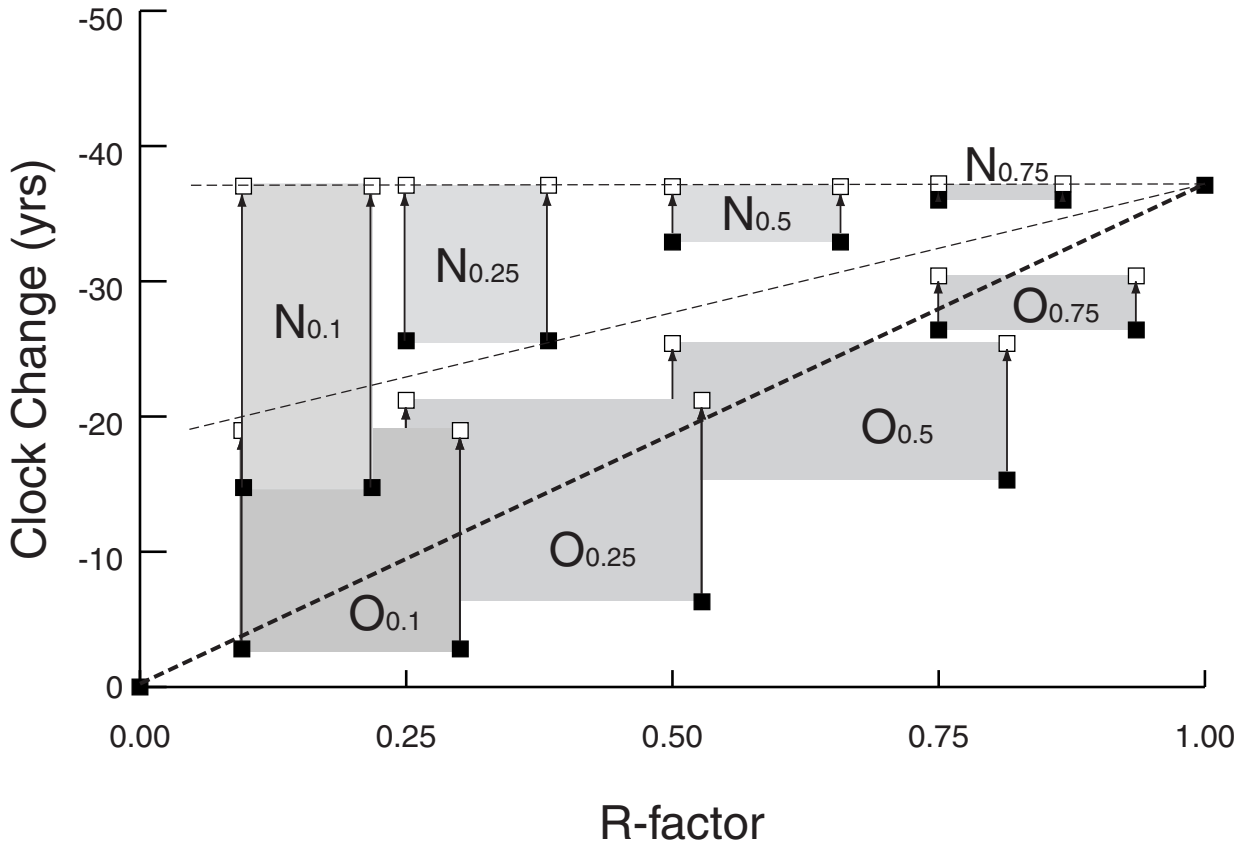
-50
-40
-30
-20
-10
0
Clock Change (yrs)
0.00
0.25
0.50
0.75
1.00
R-factor
N0.1
N0.25
N0.5
N0.75
O0.1
O0.25
O0.5
O0.75

Figure R2

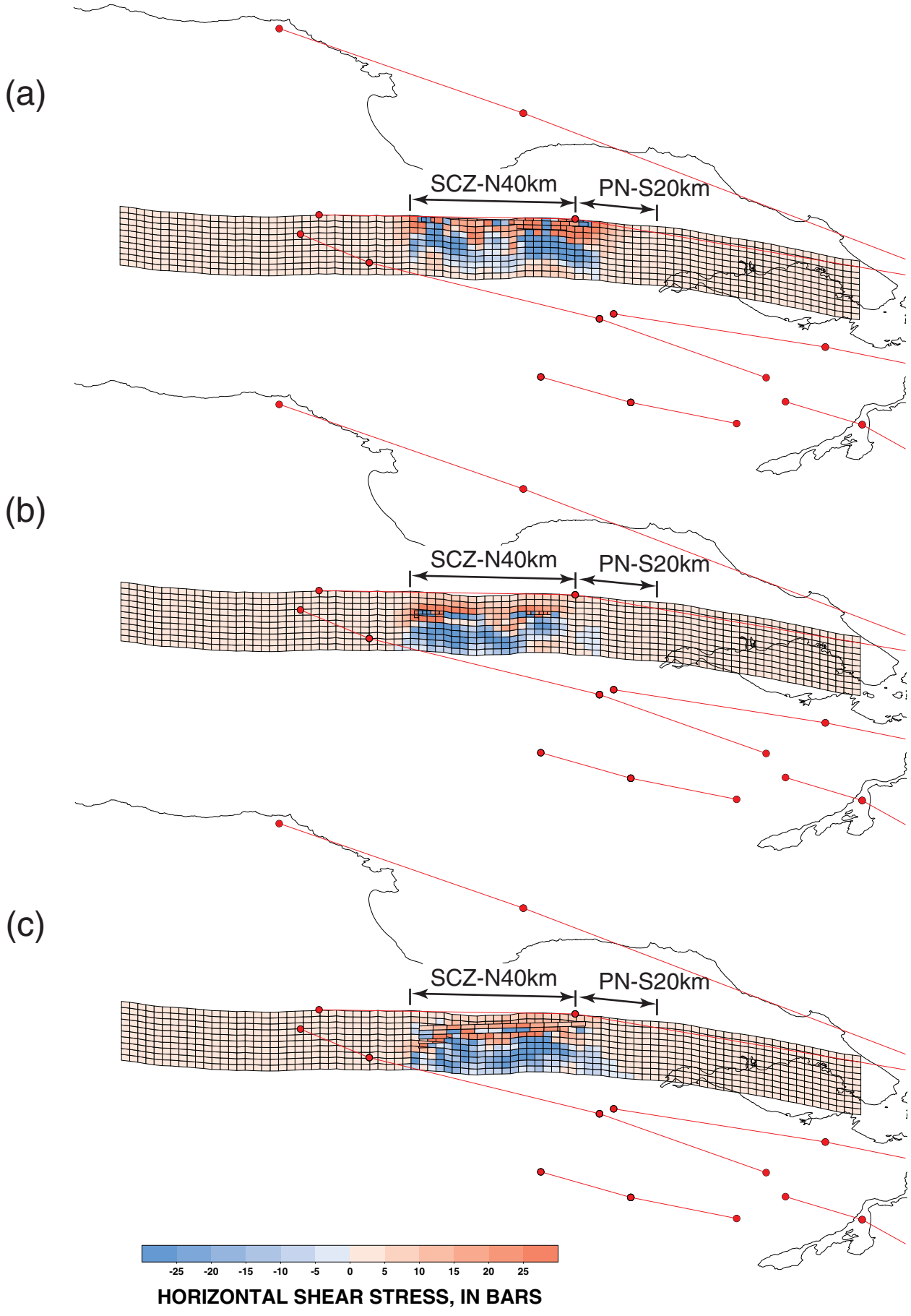
(a)
SCZ-N40km
PN-S20km
(b)
SCZ-N40km
PN-S20km
(c)
SCZ-N40km
PN-S20km
-25
-20
-15
-10
-5
0
5
10
15
20
25
HORIZONTAL SHEAR STRESS, IN BARS

Figure LP1